2D-MIMO Radar: A Method for Array Performance Assessment and Design of a Planar Antenna Array

Adolfo Di Serio, Philipp Hügler, Fabian Roos, and Christian Waldschmidt

DOI: 10.1109/TAP.2020.2972643

2-D-MIMO Radar: A Method for Array Performance Assessment and Design of a Planar Antenna Array

Adolfo Di Serio, *Student Member, IEEE*, Philipp Hügler, *Student Member, IEEE*, Fabian Roos, *Student Member, IEEE*, and Christian Waldschmidt, *Senior Member, IEEE*

***Abstract*— In this article, a method for the assessment of the performance and for the design of a 2-D-array for multiple input multiple output (2-D-MIMO) radar applications is presented. The proposed approach is based on the analysis of the ambiguity function associated with the array. Such analysis leads to the definition of an area in the 2-D-angular field-of-view of the radar, denoted as ambiguity-free region, characterized by a low probability to obtain ambiguities in direction of arrival estimation. Simulations of a basic 2-D-MIMO array are used to explain the proposed method, which is then employed as the main criterion for the optimization of a 2-D-MIMO sparse array composed of four transmitters and eight receivers. The optimization is performed through a genetic algorithm. The resulted element positions guarantee an ambiguity-free region span in the azimuth and elevation angles greater than 120° and angular resolutions of 8° and 5.9° on the azimuth and elevation angles, respectively. The optimized positions are then used to realize a 2-D-MIMO sparse array that is integrated in a radar system operating at a center frequency of 76.5 GHz. Such an array is calibrated, and comparisons between the simulated and measured ambiguity functions show the effectiveness of the proposed method.**

***Index Terms*— 2-D-array, ambiguity function, multiple input multiple output (MIMO), MIMO radar, radar.**

I. Introduction

A 3-D-IMAGING radar is able to detect the direction of the target in the azimuth and elevation angles as well as its radial distance. Such a capability may enable a wide range of possible applications. In fact, a 3-D-imaging radar has the potential to recognize the target shape in a 3-D-space [1]. This represents a key feature for applications as security body scan [2] and hidden object detection [3]. Moreover, the possibility to get angular information in both planes leads to a significant improvement of the system performance in applications as autonomous driving and drone collision avoidance [4].

Manuscript received September 26, 2019; revised January 17, 2020; accepted January 25, 2020. This work was supported by the Deutsche Forschungsgemeinschaft (DFG, German Research Foundation) under Grant WA 3506/9-1. *(Corresponding author: Adolfo Di Serio.)*

The authors are with the Institute of Microwave Engineering, Ulm University, 89081 Ulm, Germany (e-mail: adolfo.di-serio@uni-ulm.de).

Color versions of one or more of the figures in this article are available online at http://ieeexplore.ieee.org.

Digital Object Identifier 10.1109/TAP.2020.2972643

Several techniques to detect direction-of-arrival (DoA) in 3-D-space are investigated and presented in the literature, among them the most common are 2-D-beamforming [4], [5], synthetic aperture radar (SAR) [6], [7], and 2-D-multiple input multiple output (2-D-MIMO) radar [8]–[10]. Different approaches are also investigated in previous works. In [11], a system based on the combination of MIMO radar for DoA estimation on the azimuth angle and mechanical beam steering in the elevation angle is proposed. In [12], the 3-D-imaging is performed using a system composed of two orthogonal leaky wave antennas capable to perform steering of the main lobe through frequency scanning. In [13], a 3-D-imaging system based on the combination of MIMO radar and SAR is shown.

The 2-D-MIMO approach has the opportunity to provide information on the target location in a single snapshot. This procedure overcomes drawbacks such as waiting time and processing effort required to perform a complete scan of the area of interest employing 2-D-beamforming radar, SAR, mechanical scanning, frequency scanning, or combined versions of these techniques. For such a reason, this article focuses on the 2-D-MIMO array approach, how to evaluate its performance, and how to optimize antenna positions of the array.

In previous works, many efforts are made on the design of minimum redundancy MIMO arrays focusing the attention mainly on the distribution of the virtual elements of the MIMO radar. Among them, in [14], a combinatorial method to design a minimum redundancy MIMO radar with a virtual array characterized by a very large aperture for both 1-D- and 2-D-cases is proposed. In [15], two planar sparse MIMO arrays are designed using two criteria, namely the uniform distribution of the array elements and the minimization of the shadowing between virtual elements, where the latter criterion is already introduced in [16]. The simulated radiation patterns at boresight and when focused at an azimuth angle of 45° while the elevation angle is 0° are employed to evaluate the performance of the arrays.

The two cases mentioned above imply limitations. In particular, in [14], the possibility to obtain errors in the DoA process and methods to mitigate them are not taken into account. This issue is considered in [15], where a maximum sidelobe level of the radiation pattern is set in the specifications of the system. On the other hand, in [15], an evaluation of the actual

maximum sidelobe level is not performed in the optimization process, and the aforementioned simulated radiation patterns are used to evaluate the performance of the arrays only after the optimization.

An optimization method for 2-D-arrays of receivers only is presented in [17]. In particular, Lange and Yang [17] proposed an optimization of a planar array mainly based on the minimization of the Cramér–Rao bound (CRB). They claim the definition of a generalized form of the radiation pattern valid for any DoA. In such a generalized radiation pattern, the maximum sidelobe level represents a critical constraint as over this threshold it is more likely that the associated array configuration will generate ambiguities in the DoA estimation. The optimization process is limited to an application-dependent angular field-of-view.

However, in [17], there are two aspects that can be improved. The first one refers to the limitation of the analysis of the generalized beampattern to a given angular field-of-view of interest. In a practical scenario, the gain of an antenna does not sharply decay out of the angular field-of-view defined by the application. Hence, an interfering signal can be received also out of this angular region. Depending on the 2-D-array topology, this can cause ambiguities in the DoA estimation also in the field-of-view of interest. Limiting the analysis to a given angular range, this effect is neglected. The second aspect is related to the extension of the angular range of interest, which is free of ambiguities. In [17], this is characterized by the same span in both the azimuth and elevation angles. On the other hand, considering the possibility to obtain a system with an arbitrarily shaped ambiguity-free region would be beneficial for the implementation of a more general approach.

In [18], a general method for the design of a 2-D-MIMO array, similar to the one proposed in [17] but extended to the multicarrier case, is presented. However, differently from [17], Ulrich *et al.* [18] state that the evaluation of the ambiguity function for a fixed DoA is sufficient to evaluate all possible sidelobe levels and finally present the results of the optimization of a multicarrier 1-D-MIMO array. In [18], only the maximum sidelobe level of the ambiguity function associated with a fixed DoA is considered. In such a way, in case of a 2-D-array optimization, not all the information regarding the peak sidelobe level can be recognized. In fact, it can be demonstrated that depending on the array topology, there might be DoAs that produce sidelobe levels in the ambiguity function comparable to the main beam.

The authors also noticed that in the works mentioned above, where either the ambiguity function or the simulated radiation patterns are used, there is a lack of direct proof of the effectiveness of the proposed methods by the measurement results. In particular, in [15] and [17], the results of the radar imaging applications are shown. Despite that, in [15], no measured beampatterns are presented to prove, in this case, the array performance assessment method. In [17], a comparison between the simulated and measured beampatterns when focused at boresight is depicted. On the other hand, no measured beampatterns for DoAs different from the boresight are reported. That one would be necessary to give a proof of the validity of the expression of the generalized beampattern.

The work reported in this article bridges the gaps identified and highlighted in Section I. In fact, this article presents and demonstrates the effectiveness of a novel method for the performance assessment of a MIMO radar system based on a planar antenna array. Such a method is built on an extensive analysis of the full ambiguity function as defined in [19]. Thanks to this analysis, it is possible to define a region in the angular field-of-view of the radar that is characterized by a low probability to obtain ambiguities in DoA estimation, hereinafter denoted as ambiguity-free region. The analysis is performed over a span of 180° in the azimuth and elevation angles, and hence, it estimates the effect of possible interfering signals out of the field-of-view of interest for a specific application. Furthermore, the optimization method is not limited to array configurations characterized by a squared ambiguity-free region, namely with the same extension in the azimuth and elevation angles, but it also considers arrays with an arbitrarily shaped ambiguity-free region. This provides an additional degree of freedom and, hence, an augmented adaptability to the requirements of different applications. A planar MIMO array composed of four transmitters and eight receivers is optimized using a genetic algorithm that relies on the proposed method. Such an array is integrated in a radar system with a center frequency, f_c, of 76.5 GHz and then calibrated in an anechoic chamber. Unlike the relevant previous work listed above, in this article, the results of the calibration are used to evaluate the ambiguity function associated with a wide set of DoAs, which provides to the reader complete information regarding the imaging capability of the optimized array. Finally, a comparison between the measured and simulated ambiguity functions demonstrates the strong agreement between them.

This article is structured in seven sections. In Section II, the problem and the mathematical model are introduced together with the ambiguity function and the ambiguity-free region concept. A practical example of a 2-D-MIMO array to describe the performance assessment method is discussed in Section III. To this purpose, the simulated ambiguity functions are also shown. The optimization algorithm is introduced and explained in detail in Section IV. Section V shows the result of the optimization algorithm with the corresponding ambiguity function. In Section VI, the hardware with the corresponding measured ambiguity functions is reported and compared with the simulations. Section VII will conclude this article with a summary of the main outcomes.

II. Problem Definition

In this article, the conventional spherical coordinate system depicted in Fig. 1(a) is considered. The azimuth angle is denoted as φ and the elevation angle as ϑ. The planar array of transmitter and receiver elements is placed on the xz plane as it is shown in Fig. 1(b). Moreover, a radar system able to measure the position of a target in the full half-space $y > 0$ is considered. Thus, the angular coordinates will be limited in

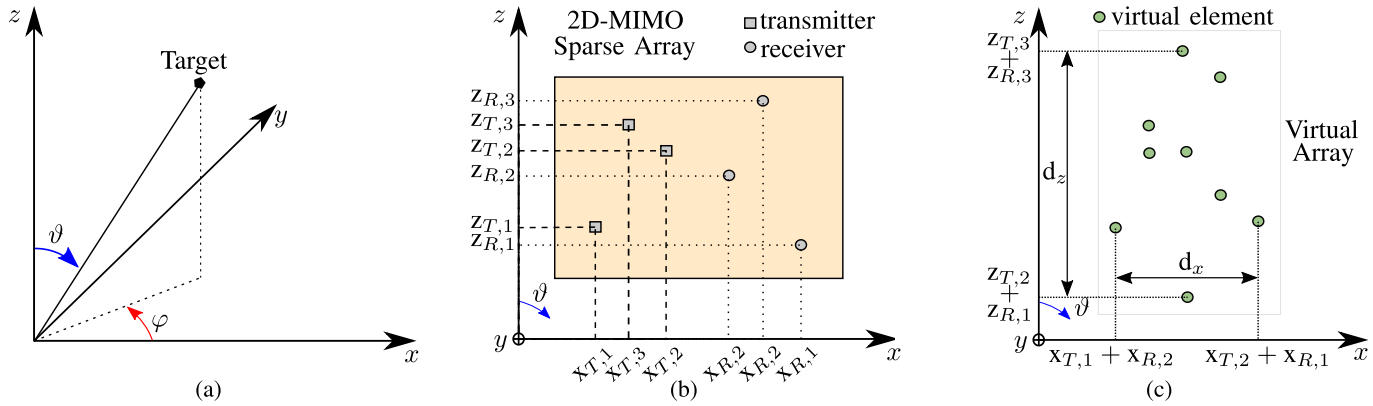

Fig. 1. Definition of the coordinate system and representation of the physical parameters of a 2-D-MIMO sparse array. (a) Spherical coordinate system. (b) Symbolic representation of a 2-D-MIMO array. (c) Associated virtual array.

the interval

$$A = \{(\varphi, \vartheta) \mid \varphi, \vartheta \in \mathbb{R}, 0 \leqslant \varphi \leqslant \pi, 0 \leqslant \vartheta \leqslant \pi\}.$$

The number of the transmitting elements is denoted as N_t, while the number of the receiving elements as N_r.

The sets of x- and z-coordinates of the transmitting element positions are denoted as

$$\mathbf{p}_{Tx} = \left(x_{T,1}\ , \ldots\ , x_{T,N_t}\right)$$
$$\mathbf{p}_{Tz} = \left(z_{T,1}\ , \ldots,\ z_{T,N_t}\right).$$

Similarly, the x- and z-coordinates of the receiving element positions are denoted as

$$\mathbf{p}_{Rx} = \left(x_{R,1}\ , \ \ldots\ , \ x_{R,N_r}\right)$$
$$\mathbf{p}_{Rz} = \left(z_{R,1}\ , \ \ldots\ , \ z_{R,N_r}\right).$$

Multistatic configurations are taken into account in this article, which means each element can act only either as a receiver or as a transmitter, but the analysis can be extended to monostatic configurations too. The employment of the MIMO technique with multiple diverse transmitted signals independent of each other is treated. In this way, it is possible to obtain a receiving steering vector composed by $N_t \times N_r$ elements denoted in the literature as a virtual steering vector [20]. Specifically, narrowband and orthogonal transmitted signals are considered to this purpose. Without loss of generality, isotropic radiating elements are taken into account.

The steering vector associated with a given DoA, (φ, ϑ), for the transmitter array can be defined as

$$\boldsymbol{a}(\varphi, \vartheta) = \begin{pmatrix} \mathrm{e}^{-\mathrm{j}\frac{2\pi}{\lambda}\left(\mathrm{x}_{T,1}\cos\varphi\sin\vartheta + \mathrm{z}_{T,1}\cos\vartheta\right)} \\ \vdots \\ \mathrm{e}^{-\mathrm{j}\frac{2\pi}{\lambda}\left(\mathrm{x}_{T,N_t}\cos\varphi\sin\vartheta + \mathrm{z}_{T,N_t}\cos\vartheta\right)} \end{pmatrix}. \tag{1}$$

Similarly, the steering vector associated with a given DoA, (φ, ϑ), for the receiver array can be defined as

$$\boldsymbol{b}(\varphi, \vartheta) = \begin{pmatrix} \mathrm{e}^{-\mathrm{j}\frac{2\pi}{\lambda}\left(\mathrm{x}_{R,1}\cos\varphi\sin\vartheta + \mathrm{z}_{R,1}\cos\vartheta\right)} \\ \vdots \\ \mathrm{e}^{-\mathrm{j}\frac{2\pi}{\lambda}\left(\mathrm{x}_{R,N_r}\cos\varphi\sin\vartheta + \mathrm{z}_{R,N_r}\cos\vartheta\right)} \end{pmatrix}. \tag{2}$$

The virtual steering vector is given by the following relation:

$$\boldsymbol{v}(\varphi, \vartheta) = \boldsymbol{a}(\varphi, \vartheta) \otimes \boldsymbol{b}(\varphi, \vartheta), \tag{3}$$

where $\otimes$ represents the Kronecker product [21]. More explicitly, the steering vector associated with the virtual array can be written as

$$\boldsymbol{v}(\varphi, \vartheta) = \begin{pmatrix} \mathrm{e}^{-\mathrm{j}\frac{2\pi}{\lambda}\left(\left(\mathrm{x}_{T,1}+\mathrm{x}_{R,1}\right)\cos\varphi\sin\vartheta + \left(\mathrm{z}_{T,1}+\mathrm{z}_{R,1}\right)\cos\vartheta\right)} \\ \vdots \\ \mathrm{e}^{-\mathrm{j}\frac{2\pi}{\lambda}\left(\left(\mathrm{x}_{T,1}+\mathrm{x}_{R,N_r}\right)\cos\varphi\sin\vartheta + \left(\mathrm{z}_{T,1}+\mathrm{z}_{R,N_r}\right)\cos\vartheta\right)} \\ \vdots \\ \mathrm{e}^{-\mathrm{j}\frac{2\pi}{\lambda}\left(\left(\mathrm{x}_{T,N_t}+\mathrm{x}_{R,1}\right)\cos\varphi\sin\vartheta + \left(\mathrm{z}_{T,N_t}+\mathrm{z}_{R,1}\right)\cos\vartheta\right)} \\ \vdots \\ \mathrm{e}^{-\mathrm{j}\frac{2\pi}{\lambda}\left(\left(\mathrm{x}_{T,N_t}+\mathrm{x}_{R,N_r}\right)\cos\varphi\sin\vartheta + \left(\mathrm{z}_{T,N_t}+\mathrm{z}_{R,N_r}\right)\cos\vartheta\right)} \end{pmatrix}. \tag{4}$$

The x- and z-coordinates of its elements are denoted as

$$\mathbf{p}_{Vx} = \begin{pmatrix} \mathrm{x}_{T,1} + \mathrm{x}_{R,1} \\ \vdots \\ \mathrm{x}_{T,1} + \mathrm{x}_{R,N_r} \\ \vdots \\ \mathrm{x}_{T,N_t} + \mathrm{x}_{R,1} \\ \vdots \\ \mathrm{x}_{T,N_t} + \mathrm{x}_{R,N_r} \end{pmatrix}, \quad \mathbf{p}_{Vz} = \begin{pmatrix} \mathrm{z}_{T,1} + \mathrm{z}_{R,1} \\ \vdots \\ \mathrm{z}_{T,1} + \mathrm{z}_{R,N_r} \\ \vdots \\ \mathrm{z}_{T,N_t} + \mathrm{z}_{R,1} \\ \vdots \\ \mathrm{z}_{T,N_t} + \mathrm{z}_{R,N_r} \end{pmatrix}.$$

The apertures of the virtual array in the x- and z-dimensions are defined as

$$d_x = \max\left(\mathbf{p}_{Vx}\right) - \min\left(\mathbf{p}_{Vx}\right) \tag{5}$$
$$d_z = \max\left(\mathbf{p}_{Vz}\right) - \min\left(\mathbf{p}_{Vz}\right). \tag{6}$$

In order to introduce the next concepts, the interval A can be discretized and renamed as

$$A_d = \{\left(\varphi_i, \vartheta_j\right) \mid \varphi_i, \vartheta_j \in \mathbb{R}, \quad i, j \in \mathbb{N}, \quad 0 \leqslant \varphi_i \leqslant \pi$$
$$0 \leqslant \vartheta_j \leqslant \pi, \quad i = 1, \ldots, N, \quad j = 1, \ldots, M\}$$

where N and M are the number of possible different DoAs in the azimuth and elevation angles, respectively.

According to the definition of the ambiguity function presented in [19], in this article, the ambiguity function for 2-D-MIMO arrays is defined as

$$\chi\left(\varphi_i^r, \vartheta_j^r, \varphi_k^e, \vartheta_l^e\right) = \frac{\boldsymbol{v}^\dagger(\varphi_i^r, \vartheta_j^r) \cdot \boldsymbol{v}(\varphi_k^e, \vartheta_l^e)}{\|\boldsymbol{v}^\dagger(\varphi_i^r, \vartheta_j^r)\| \|\boldsymbol{v}(\varphi_k^e, \vartheta_l^e)\|} \tag{7}$$

with

$$i, k = 1, \ldots, N, \quad j, l = 1, \ldots, M$$

and

$$\chi\left(\varphi_i^r, \vartheta_j^r, \varphi_k^e, \vartheta_l^e\right) \in [0, 1].$$

In (7), the superscript r is used to indicate the real DoAs and the superscript e to indicate estimated ones.

The analysis of the ambiguity function as defined in (7) is not trivial as it depends on four variables, namely φ_i^r, ϑ_j^r, φ_k^e, and ϑ_l^e. In spite of that, it is possible to transform this 4-D-problem into a 2-D one. Let $\mathbf{X}_{ij}$ be the ambiguity function matrix associated with a real DoA, $(\varphi_i^r, \vartheta_j^r)$, which is defined as

$$\mathbf{X}_{ij} = \begin{pmatrix} \chi(\varphi_i^r, \vartheta_j^r, \varphi_1^e, \vartheta_1^e) & \ldots & \chi(\varphi_i^r, \vartheta_j^r, \varphi_1^e, \vartheta_M^e) \\ \vdots & \vdots & \vdots \\ \chi(\varphi_i^r, \vartheta_j^r, \varphi_N^e, \vartheta_1^e) & \ldots & \chi(\varphi_i^r, \vartheta_j^r, \varphi_N^e, \vartheta_M^e) \end{pmatrix} \tag{8}$$

with

$$\mathbf{X}_{ij} \in [0, 1]^{N \times M}.$$

Considering a 2-D-MIMO array with element positions depicted in Fig. 2, the corresponding ambiguity function matrix associated with a real DoA, $(\varphi^r, \vartheta^r) = (90°, 90°)$, hence, $\mathbf{X}(\varphi^r = 90°, \vartheta^r = 90°)$, is reported in Fig. 3(a).

As a first step, it is necessary to calculate the matrices associated with every pair $(\varphi_i^r, \vartheta_j^r)$ of real DoAs. These ambiguity function matrices can be used to build an ambiguity function hypermatrix $\mathbf{H}$ defined as

$$\mathbf{H} = \left[\ \mathbf{X}_{ij}\ \right] \tag{9}$$

with

$$\mathbf{H} \in [0, 1]^{N^2 \times M^2}.$$

Also, in this case, considering the 2-D-MIMO array in Fig. 2, an example of a reduced version, the corresponding ambiguity function hypermatrix with $\varphi^r, \vartheta^r \in \{0°, 30°, \ldots, 180°\}$ is depicted in Fig. 3(d).

The ambiguity function hypermatrix $\mathbf{H}$ as it is stated in (9) contains all the information of the ambiguity function defined in (7).

The ambiguity function matrix $\mathbf{X}_{ij}$, in general, is characterized by a region with high autocorrelation values in the neighborhood of the associated DoA $(\varphi_i^r, \vartheta_j^r)$ and by several local maxima. The highest local maxima of $\mathbf{X}_{ij}$ is defined as the maximum sidelobe level, and it is denoted as $\mathrm{SLL}_{\max}(\varphi_i^r, \vartheta_j^r)$. This is a critical parameter as it is often used to evaluate the probability of errors in the DoA estimation [18]. By defining a maximum threshold t for the peak sidelobe level of $\mathbf{X}_{ij}$, it is possible to determine for which pair $(\varphi_i^r, \vartheta_j^r)$ there is a high probability to obtain ambiguities in the DoA estimation. In particular, this case occurs when the maximum sidelobe level of the ambiguity function $\mathrm{SLL}_{\max}(\varphi_i^r, \vartheta_j^r) > t$. By performing such a check for all the possible DoAs, we can define an ambiguity indicator matrix as

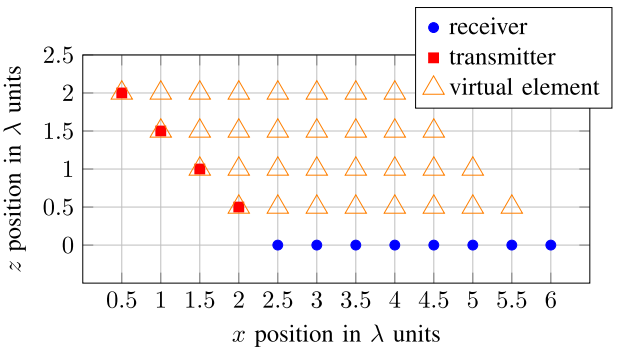

Fig. 2. Positions of the basic 2-D-MIMO array elements with four transmitters and eight receivers.

$$\mathbf{Q} = \left[\ \mathrm{Q}_{ij}\ \right] \tag{10}$$

with

$$\mathrm{Q}_{ij} = \begin{cases} 0, & \mathrm{SLL}_{\max}(\varphi_i^r, \vartheta_j^r) \le t \\ 1, & \mathrm{SLL}_{\max}(\varphi_i^r, \vartheta_j^r) > t \end{cases} \tag{11}$$

and

$$\mathbf{Q} \in \{0, 1\}^{N \times M}.$$

The pairs $(\varphi_i^r, \vartheta_j^r)$ for which $\mathrm{Q}_{i,j} = 0$ define the ambiguity-free region. In the following analysis, a threshold for the peak sidelobe level $t = 0.5 = -6$ dB is considered.

An estimation of the angular resolution of the MIMO array in the azimuth and elevation angles is calculated using the Rayleigh criterion [22]. In particular, they are defined, respectively, as

$$\Delta\varphi = 1.22\frac{\lambda}{d_x} \tag{12}$$

$$\Delta\vartheta = 1.22\frac{\lambda}{d_z}. \tag{13}$$

III. MIMO Array Performance Assessment

The performance assessment is mainly based on the concepts of ambiguity-free region and angular resolution. To explain the method used to evaluate the performance of a 2-D-MIMO array, a practical example is proposed. In particular, a 2-D-MIMO array characterized by four transmitters and eight receivers is considered.

The positions of the transmitter and receiver elements are listed in Tables I and II, respectively. The virtual array is composed by $4 \times 8 = 32$ elements and it is depicted in Fig. 2 together with the transmitter and receiver positions. The virtual apertures on the x- and z-dimensions are $d_x = 5\lambda$ and $d_z = 1.5\lambda$, respectively. Thus, the estimated angular resolutions of this MIMO array in the azimuth and elevation angles are $\Delta\varphi = 15.5°$ and $\Delta\vartheta = 46.6°$, respectively.

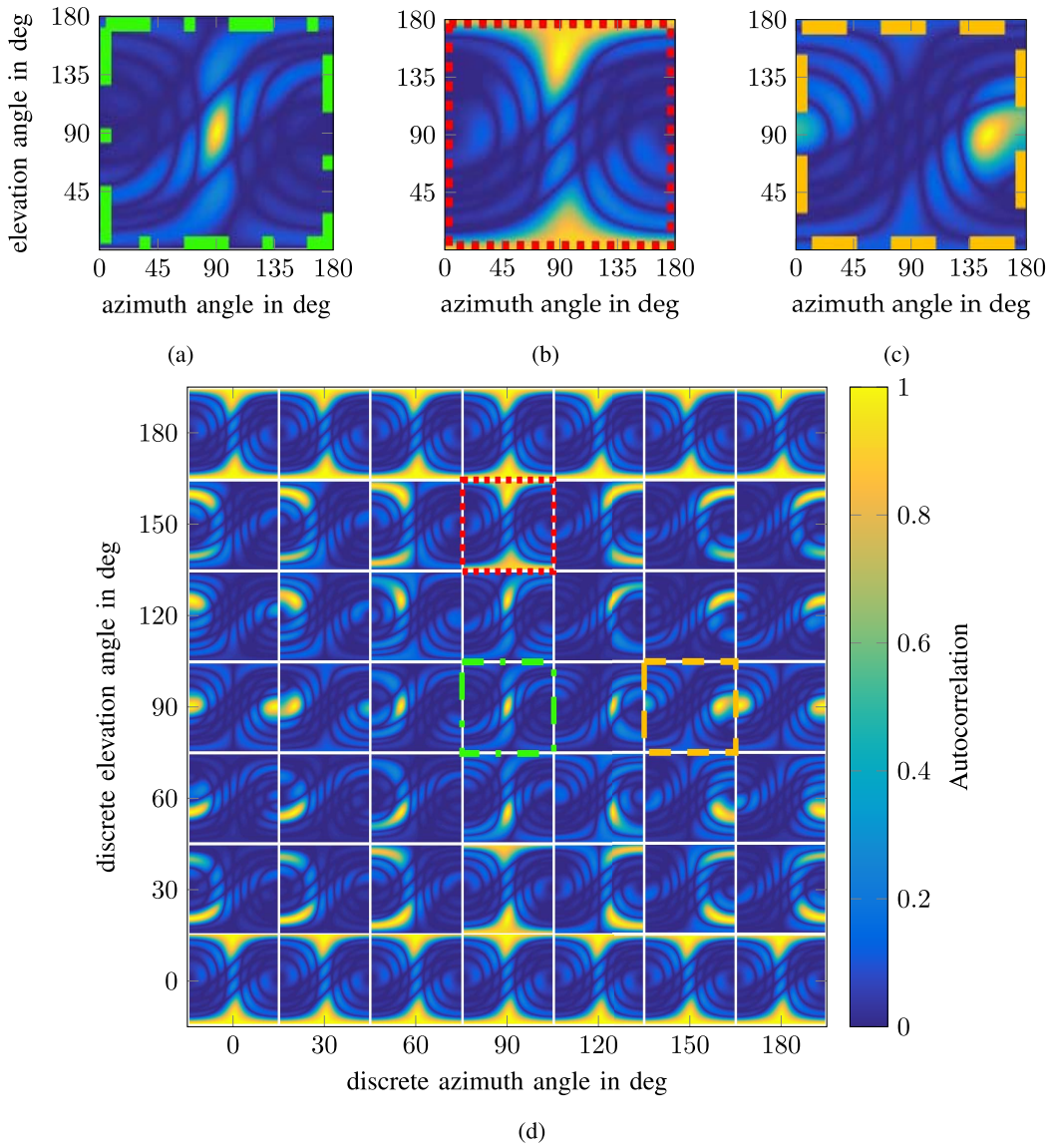

Fig. 3. Ambiguity function plots associated with the basic 2-D-MIMO array. (a) $\mathbf{X}(\varphi^r = 90°, \vartheta^r = 90°)$. (b) $\mathbf{X}(\varphi^r = 90°, \vartheta^r = 150°)$. (c) $\mathbf{X}(\varphi^r = 150°, \vartheta^r = 90°)$. (d) Reduced ambiguity function hypermatrix $\mathbf{H}$ with $\varphi^r, \vartheta^r \in \{0°, 30°, \ldots, 180°\}$.

TABLE I
TRANSMITTER POSITIONS OF THE BASIC 2-D-MIMO ARRAY

i	1	2	3	4
$x_{T,i}$ in λ	2	1.5	1	0.5
$z_{T,i}$ in λ	0.5	1	1.5	2

TABLE II
RECEIVER POSITIONS OF THE BASIC 2-D-MIMO ARRAY

i	1	2	3	4	5	6	7	8
$x_{R,i}$ in λ	2.5	3	3.5	4	4.5	5	5.5	6
$z_{R,i}$ in λ	0	0	0	0	0	0	0	0

The ambiguity function matrix $\mathbf{X}(\varphi^r = 90°, \vartheta^r = 90°)$ associated with this MIMO array for a hypothetical real DoA in the boresight direction is shown in Fig. 3(a). In this plot, the x-axis represents the set of estimated azimuth angles φ_k^e, while the y-axis represents the set of estimated elevation angles ϑ_l^e. As this plot is associated with the real DoA, $(\varphi^r, \vartheta^r) = (90°, 90°)$, in the ideal case, the main high correlation region is expected to be in the neighborhood of the pair $(\varphi^e, \vartheta^e) = (90°, 90°)$, which represents the main beam and low correlation values in the surrounding region. The plot in Fig. 3(a) satisfies such an expectation and highlights that the maximum sidelobe level of the ambiguity function is $\mathrm{SLL}_{\max}(90°, 90°) = 0.26 = -11.7$ dB.

A reduced version of the ambiguity function hypermatrix $\mathbf{H}$ with $\varphi^r, \vartheta^r \in \{0°, 30°, \ldots, 180°\}$, is depicted in Fig. 3(d). In this plot, discrete sets of values of φ_i^r and ϑ_j^r are depicted on the horizontal axis and on the vertical axis, respectively. Associated with each pair of $(\varphi_i^r, \vartheta_j^r)$, the respective ambiguity function matrix $\mathbf{X}_{ij}$ is plotted, and on these plots, two subsets of φ_k^e, and ϑ_l^e, with $k = 1, \ldots, N$ and $l = 1, \ldots, M$, need to be considered on the horizontal axis and on the vertical axis, respectively.

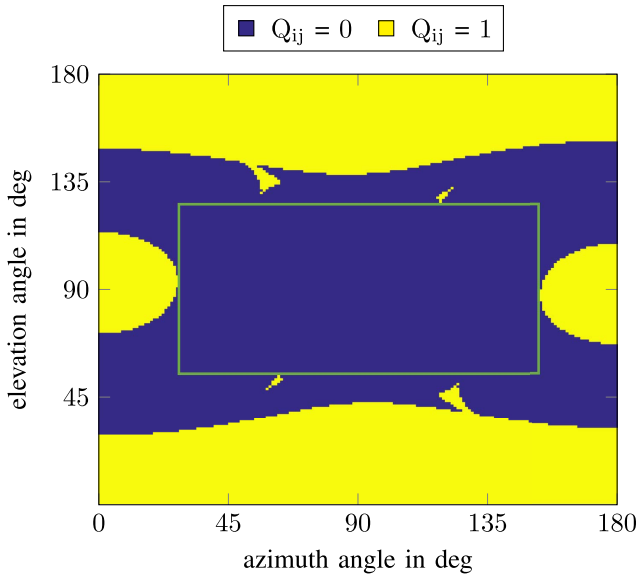

Fig. 4. Ambiguity indicator matrix **Q** of the basic 2-D-MIMO array with four transmitters and eight receivers.

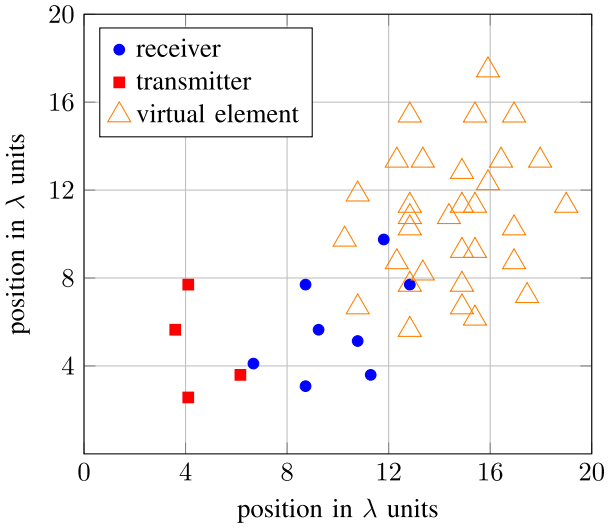

Fig. 5. Position of the optimized 2-D-MIMO sparse array elements with four transmitters and eight receivers.

To facilitate the understanding of the ambiguity function hypermatrix plot in Fig. 3(d), it can be noticed that the ambiguity function matrix $\mathbf{X}(\varphi^r = 90°, \vartheta^r = 90°)$ in Fig. 3(a) is corresponding to the real DoA, $(\varphi^r, \vartheta^r) = (90°, 90°)$ and highlighted with a green dash-dotted square. In Fig. 3(b) and (c), the ambiguity function matrices $\mathbf{X}(\varphi^r = 90°, \vartheta^r = 150°)$, $\mathbf{X}(\varphi^r = 150°, \vartheta^r = 90°)$ are also plotted. These plots can be mapped in the reduced ambiguity function hypermatrix in correspondence of the real DoA $(\varphi^r, \vartheta^r) = (90°, 150°)$ that is highlighted with a red dotted square, and $(\varphi^r, \vartheta^r) = (150°, 90°)$ that is highlighted with an orange dashed square. In the reduced ambiguity function hypermatrix plot, it can also be observed how the main beam is steered accordingly to the pair of real DoAs, $(\varphi_i^r, \vartheta_j^r)$, and how the ambiguities occur at the edges of the sets, where more regions with high correlation values appear on the same ambiguity function matrix. An example of the latter effect can be observed in Fig. 3(b).

The ambiguity indicator matrix **Q** is depicted in Fig. 4. The yellow area represents the real DoA values where the associated ambiguity function matrix presents $\mathrm{SLL}_{\max}(\varphi_i^r, \vartheta_j^r) > t$, the blue area represents the real DoA values where the $\mathrm{SLL}_{\max}(\varphi_i^r, \vartheta_j^r) \leq t$. In this plot, it can be seen that the basic array is characterized by an arbitrarily shaped ambiguity-free region. The regular shape with maximum extension that groups a contiguous area in the neighborhood of the boresight with low probability to obtain ambiguities, hereinafter denoted as contiguous ambiguity-free region, is a rectangle. This means that its extension on the azimuth plane is different from the one in the elevation plane. In this specific case, the contiguous ambiguity-free region is in the range of $27° \leq \varphi^r \leq 153°$, $54° \leq \vartheta^r \leq 126°$ and it is highlighted by the green box inside the plot in Fig. 4.

IV. 2-D-MIMO Sparse Array Optimization

In order to validate the method for the 2-D-MIMO array performance assessment and to improve the angular resolution and the extension of the ambiguity-free region with respect to the previous example, a 2-D-MIMO sparse array is optimized. Concerning the transmitter and receiver elements, an array of four patch antennas with parallel feeding is considered. The proposed method for 2-D-MIMO radar performance assessment is used as the main criterion for the optimization, and it is implemented in a genetic algorithm whose flowchart is introduced in [23]. In the genetic algorithm that is specialized for a 2-D-MIMO radar optimization, a gene represents the antenna element position on the plane. Sets of $N_t + N_r$ genes represent a single full 2-D-MIMO array configuration, which is a chromosome. A set of twelve chromosomes forms the population. The constraints applied in the algorithm are summarized in the following points.

1) The maximum area available for the array elements is 80 mm × 80 mm.
2) The single-element dimension amounts to 2.88 mm × 3 mm.
3) A discrete set of positions is available, namely a grid with 2 mm ($> \lambda/2$) spacing in the x- and y-directions, which is required to perform a 2-D-discrete Fourier transform (2-D-DFT)-based DoA estimation.
4) No overlap between elements of the physical array is allowed.
5) No overlap between virtual elements is allowed in order to maximize the number of virtual elements available and, hence, to increase the extension of the virtual aperture.
6) The contiguous ambiguity-free region must be larger than $30° \leq \varphi^r \leq 150°$, $30° \leq \vartheta^r \leq 150°$.
7) The maximum threshold for peak sidelobe levels is $t = 0.5 = -6$ dB.

For each chromosome, a cost function is calculated, which is inversely proportional to the extension of the ambiguity-free region. Moreover, in the cost function, a higher weight to the angular region in the interval $30° \leq \varphi^r \leq 150°$, $30° \leq \vartheta^r \leq 150°$ is given. In order to provide a symbolic

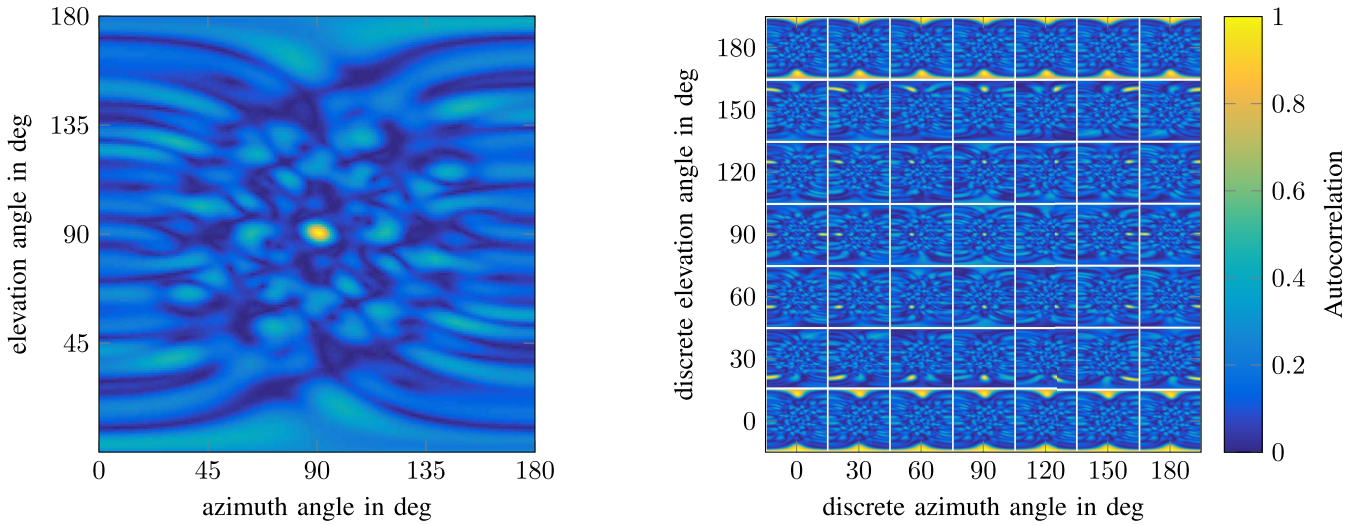

(a) (b)

Fig. 6. Ambiguity function plots associated with the optimized 2-D-MIMO sparse array. (a) $\mathbf{X}(\varphi^r = 90°, \vartheta^r = 90°)$. (b) $\mathbf{H}$ with $\varphi^r, \vartheta^r \in \{0°, 30°, \ldots, 180°\}$.

TABLE III
POSITIONS OF THE 2-D-MIMO SPARSE ARRAY TRANSMITTERS

i	1	2	3	4
$x_{T,i}$ in λ	3.57	4.08	4.08	6.12
$z_{T,i}$ in λ	5.61	2.55	7.65	3.57

TABLE IV
POSITIONS OF THE 2-D-MIMO SPARSE ARRAY RECEIVERS

i	1	2	3	4	5	6	7	8
$x_{R,i}$ in λ	6.63	8.67	8.67	9.18	10.71	11.22	11.73	12.75
$z_{R,i}$ in λ	4.08	7.65	3.06	5.61	5.1	3.57	9.69	7.65

expression of the cost function, $A(\varphi_i^r, \vartheta_j^r, \varphi_k^e, \vartheta_l^e)$ is defined as a ratio. The numerator is the number of elements of $\mathbf{X}_{ij}$ which are greater than t, with $30° \leq \varphi^e \leq 150°$ and $30° \leq \vartheta^e \leq 150°$, excluding the elements representing the main beam. The denominator is $N \times M$. Similarly, $B(\varphi_i^r, \vartheta_j^r, \varphi_k^e, \vartheta_l^e)$ is defined also as a ratio. In this case, the numerator is the number of elements of $\mathbf{X}_{ij}$ which are greater than t, with $0° \leq \varphi^e \leq 180°$ and $0° \leq \vartheta^e \leq 180°$, excluding the main beam, and the denominator is $N \times M$. The cost function is defined as

$$f(\varphi_i^r, \vartheta_j^r, \varphi_k^e, \vartheta_l^e) = \sum_{i=1}^{N}\sum_{j=1}^{M}\big(A(\varphi_i^r, \vartheta_j^r, \varphi_k^e, \vartheta_l^e) + c_1 B(\varphi_i^r, \vartheta_j^r, \varphi_k^e, \vartheta_l^e) + c_2 \mathrm{SLL}_{\max}(\varphi_i^r, \vartheta_j^r)\big) \quad (14)$$

where $c_1 = 1/4$ and $c_2 = 3/4$.

As the objective is to increase the extension of the ambiguity-free region and the aperture of the array, the goal is to minimize the cost function value.

V. OPTIMIZED 2-D-MIMO SPARSE ARRAY

The positions of the transmitter and receiver elements of the optimized 2-D-MIMO sparse array are listed in Tables III and IV, respectively. The transmitter, receiver, and virtual element positions of the optimized array are depicted in Fig. 5.

Considering the same amount of elements with respect to the 2-D-array presented in Section III, the 2-D-MIMO sparse array shows a significant improvement in terms of angular resolution in both the azimuth and elevation angles. In particular, the aperture of the virtual array in the x- and z-directions are $d_x = 8.67\lambda$ and $d_z = 11.73\lambda$, respectively, and hence, the estimated angular resolutions in the azimuth and elevation angles are $\Delta\varphi = 8°$ and $\Delta\vartheta = 5.9°$, respectively. In Fig. 6(a), the plot of the ambiguity function matrix for a real DoA at boresight $\mathbf{X}(\varphi^r = 90°, \vartheta^r = 90°)$ is reported. In this plot, in comparison with the plot in Fig. 3(a), a narrower main

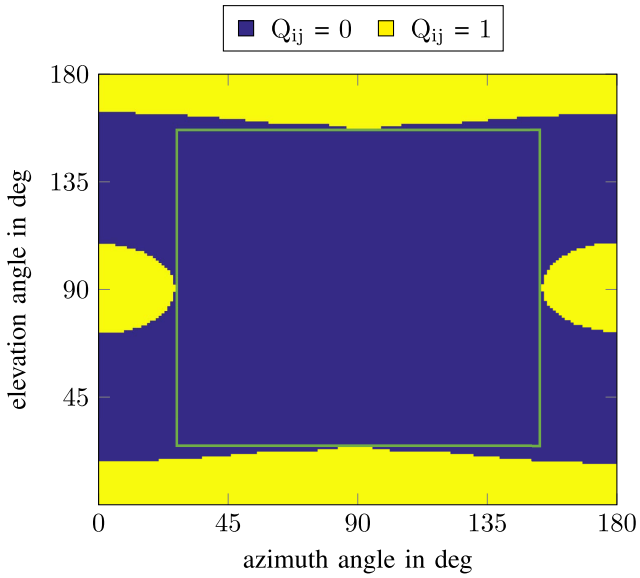

Fig. 7. Ambiguity indicator matrix $\mathbf{Q}$ of the optimized 2-D-MIMO sparse array with four transmitters and eight receivers.

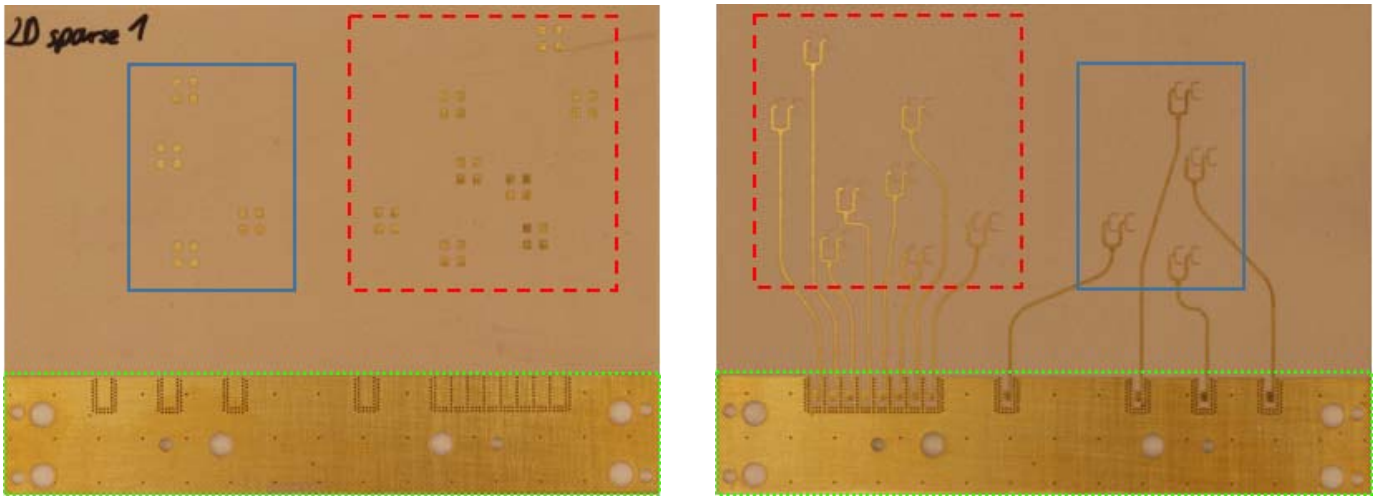

(a) (b)

Fig. 8. Optimized 2-D-MIMO sparse array frontend with four transmitter antennas and eight receiver antennas. (a) Front view. (b) Back view.

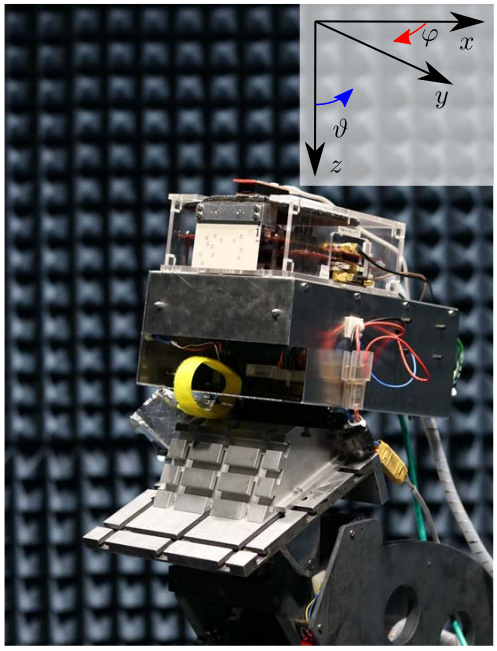

Fig. 9. Measurement setup for the calibration of the optimized 2-D-MIMO sparse array.

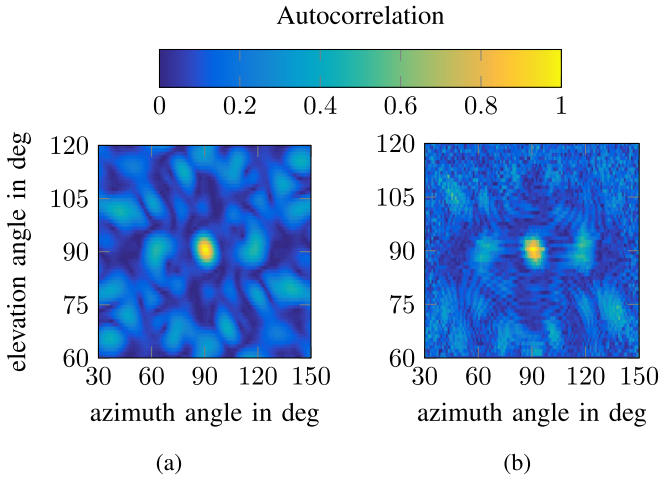

(a) (b)

Fig. 10. Plot of the ambiguity function matrix associated with the optimized 2-D-MIMO sparse array for a real DoA at the boresight. (a) Simulated $\mathbf{X}(\varphi^r = 90°, \vartheta^r = 90°)$. (b) Measured $\mathbf{X}^m(\varphi^r = 90°, \vartheta^r = 90°)$.

beam can be noticed. The maximum sidelobe level of the ambiguity function is $\mathrm{SLL}_{\max}(90°, 90°) = 0.46 = -6.75$ dB.

In Fig. 6(b) a reduced version of the ambiguity function hypermatrix $\mathbf{H}$ with $\varphi^r, \vartheta^r \in \{0°, 30°, \ldots, 180°\}$ is depicted. By comparing this plot to Fig. 3(d), it can be observed that the optimized array produces higher sidelobe levels in the neighborhood of the boresight direction. On the other hand, they do not exceed the threshold t in a larger region of the angular field-of-view. In particular, analyzing the ambiguity indicator matrix $\mathbf{Q}$ that is plotted in Fig. 7, it can be observed that the optimized array is characterized by a contiguous rectangular ambiguity-free region in the neighborhood of the boresight, which is wider than the one presented in Fig. 4. Specifically, it is in the range $23° \leq \varphi^r \leq 157°$, $26° \leq \vartheta^r \leq 154°$, which is also highlighted by the green box inside the plot in Fig. 7.

The performance analysis of the optimized 2-D-MIMO array highlights that the array element positions obtained from the genetic algorithm based on the proposed assessment criterion fully meet the system requirements and satisfy the constraints that are listed in Section IV. In addition, the proposed optimization method based on the extensive analysis of the ambiguity function takes into account the real DoA in the full angular field-of-view, i.e., in the range $0° \leq \varphi^r \leq 180°$, $0° \leq \vartheta^r \leq 180°$. This overcomes limitations identified in previous works, where either the maximum sidelobe level of the ambiguity function at boresight or in a limited field-of-view for a specific application is considered. In such a way, the effect of interfering signals outside the angular field-of-view is neglected. With the approach proposed in this article, this effect is taken into account, conferring to

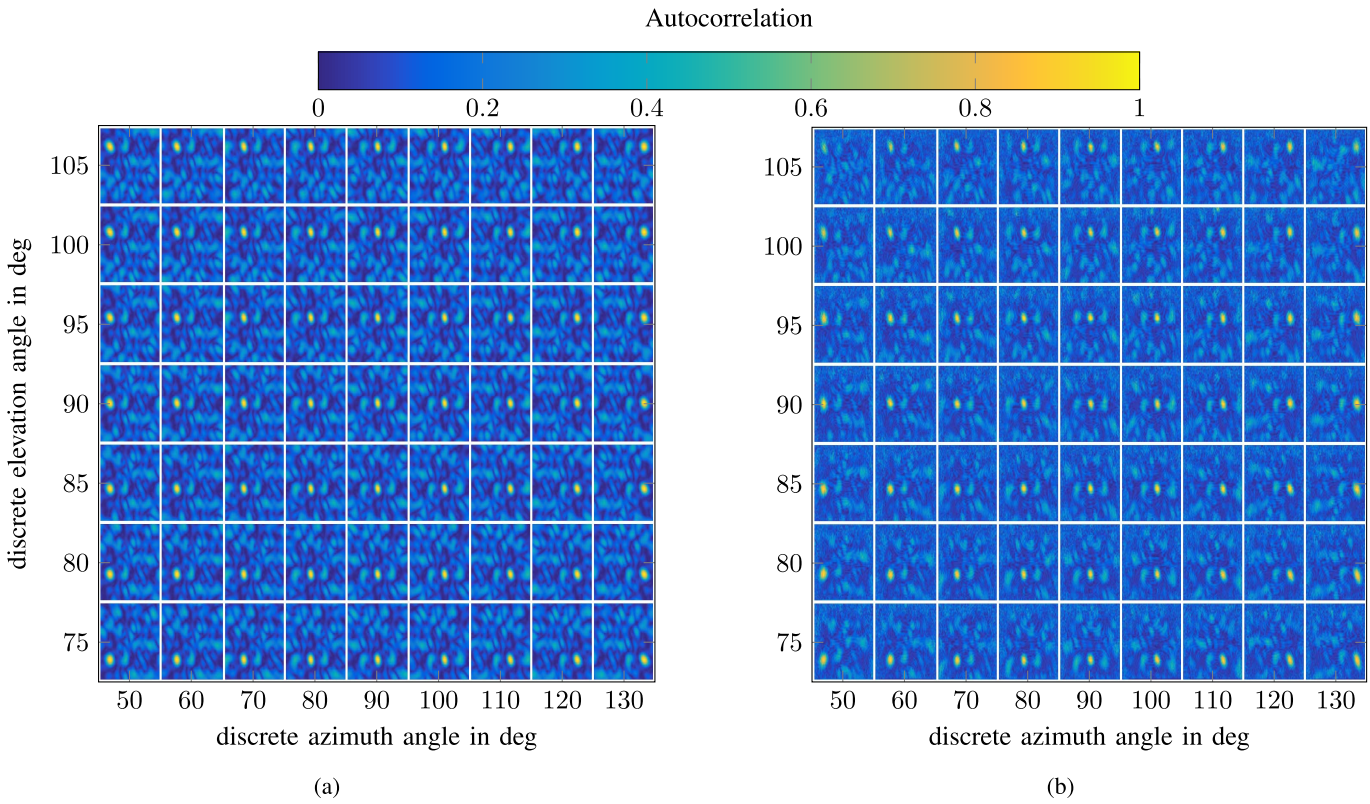

Fig. 11. Plot of the reduced ambiguity function hypermatrix with $\varphi^r \in \{50°, 60°, \ldots, 130°\}$ and $\vartheta^r \in \{75°, 80°, \ldots, 105°\}$. (a) Simulated $\mathbf{H}$. (b) Measured $\mathbf{H}^m$.

the optimized array an improved reliability in terms of DoA estimation with respect to solutions that are proposed so far in the literature.

VI. System Demonstrator

In order to demonstrate the effectiveness of the proposed method, the optimized 2-D-MIMO sparse array is fabricated. A picture of the antenna array frontend is reported in Fig. 8.

The antenna element is composed by an array of four patch antennas with parallel feeding. The feeding of the single patch antenna is implemented through the aperture coupling technique. The spacing between the patch antennas is $\lambda/2$ on both dimensions, so that the antenna array presents similar radiation characteristics in the E- and H-planes. Specifically, the antenna element is characterized by a peak realized gain at 76.5 GHz of 11 dBi and a half power beamwidth (HPBW) of approximately 45° in the E- and H-planes.

As for the 2-D-MIMO sparse array, in Fig. 8(a) and (b), it can be observed that the four transmitters are grouped on the left side in the blue solid square, while the eight receivers are grouped on the right side in the red dashed square. The dimensions of this board are 80 mm $\times$ 60 mm. The hardware of the imaging radar used to this purpose is described in [24].

The array calibration is performed in an anechoic chamber placing a corner reflector with the radar cross section (RCS) of 4.5 dBsm at a distance of 5 m from the antenna array. Measurements of the target are taken by rotating the antenna array around its phase center over both the azimuth and elevation angles with steps of 1°. Fig. 9 shows the measurement setup that is used for the calibration process. The 2-D-MIMO sparse array is connected to the radar transceiver through the microstrip to rectangular waveguide transition. The whole system is placed on a turning table that is able to rotate in the azimuth and elevation angles. A reference coordinate system in Fig. 9 indicates their orientation. The angular range where to perform the calibration is established according to the radiation characteristics of the antenna element. In particular, the antenna HPBW defines the minimum angular field-of-view of the radar system. The angular field-of-view can go beyond these values depending on the antenna radiation pattern and, hence, on the signal-to-noise ratio (SNR) at the receiver. For this reason, the calibrated angular region is limited to directions where the antenna gain presents a decay within 20 dB with respect to the maximum value. This angular range covers a span of 120° in the azimuth and elevation angles. However, the measurement setup can perform a rotation in the elevation angle within a span of 60°. This leads to a calibration on the azimuth angle in the range $30° \leq \varphi^r \leq 150°$, while on the elevation angle in the range $60° \leq \vartheta^r \leq 120°$.

In the calibration process, a block of 256 ramp signals is transmitted. For each virtual receiving channel, the received beat signal is processed through the application of a 2-D-DFT to obtain a range–velocity matrix for each virtual receiving channel. The results of the 2-D-DFT for each channel are then accumulated in one range–velocity matrix through a noncoherent integration so that the SNR can be increased.

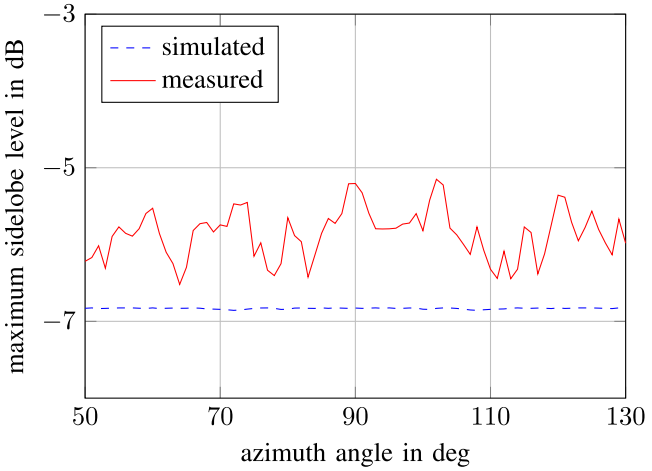

Fig. 12. Plot of the simulated and measured maximum sidelobe levels $\mathrm{SLL}_{\max}(\varphi_i^r, \vartheta_j^r)$ and $\mathrm{SLL}_{\max}^m(\varphi_i^r, \vartheta_j^r)$ for $50° \leq \varphi^r \leq 130°$ and $\vartheta^r = 90°$.

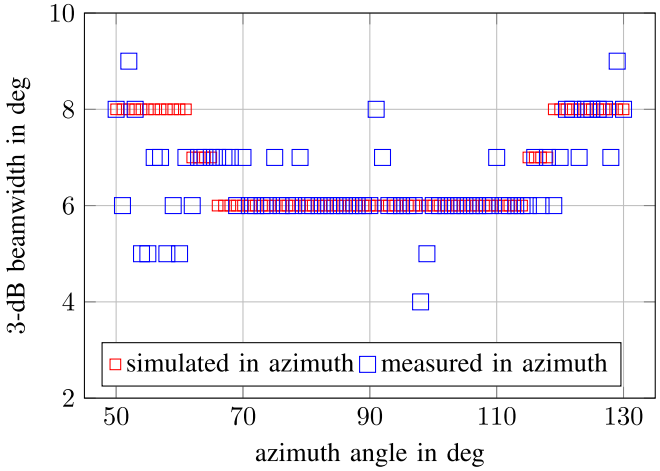

Fig. 13. Plot of the simulated and measured HPBW, $\mathrm{HPBW}(\varphi_i^r, \vartheta_j^r)$ and $\mathrm{HPBW}^m(\varphi_i^r, \vartheta_j^r)$, in the azimuth angle for $50° \leq \varphi^r \leq 130°$ and $\vartheta^r = 90°$.

An ordered-statistics constant false alarm rate (OS-CFAR) algorithm [25] is then applied to the accumulated matrix to get the range–velocity cell of the target. Finally, with knowledge of the last item, it is possible to go back to the range–velocity matrices associated with each virtual receiving channel. By taking the phase of the target range–velocity cell in each receiver range–velocity matrix, the steering vector associated with the specific DoA value can be obtained.

The measured ambiguity function for the 2-D-MIMO sparse array is calculated through the calibration matrix $\boldsymbol{v}^m(\varphi_i^r, \vartheta_j^r)$, with $i = 1, \ldots, 121$ and $j = 1, \ldots, 61$, using (7). In Fig. 10(a) and (b), the simulated and measured ambiguity function matrices, $\mathbf{X}(\varphi^r = 90°, \vartheta^r = 90°)$ and $\mathbf{X}^m(\varphi^r = 90°, \vartheta^r = 90°)$, associated with a real DoA at boresight are shown. A strong agreement between these two plots can be noticed. In particular, it can be observed that the maximum position of the main beam is the same in both plots, namely in correspondence of $(\varphi^e, \vartheta^e) = (90°, 90°)$. The HPBW in the azimuth and elevation angles is also the same for both plots with 6° and 4°, respectively. Moreover, the sidelobe levels are comparable as in the measured ambiguity function matrix, the maximum sidelobe level is $0.55 = -5.19$ dB, while in the simulated one, it is $0.46 = -6.75$ dB.

In Fig. 11(a) and (b), the simulated and measured ambiguity function hypermatrices, $\mathbf{H}$ and $\mathbf{H}^m$, respectively, are reported. In order to compare the two plots, an analysis on the maximum sidelobe level for the simulated and measured cases is performed. In Fig. 12, a plot of the simulated $\mathrm{SLL}_{\max}(\varphi_i^r, \vartheta_j^r)$ (- - -) and of the measured $\mathrm{SLL}_{\max}^m(\varphi_i^r, \vartheta_j^r)$ (——) with $30° \leq \varphi^r \leq 150°$, and $\vartheta^r = 90°$ is depicted. In the measured ambiguity function matrices, a few high autocorrelation points can occur at the edge of the angular field-of-view. This is due to possible reflections caused by the metal part of the microstrip line to rectangular waveguide transitions that is in proximity to the antennas. In particular, this item allows the mechanical connection of the array frontend to the rectangular waveguides, and it is mounted on front and back sides of the antenna frontend in correspondence of the green dotted square in Fig. 8(a) and (b). In order to mitigate the

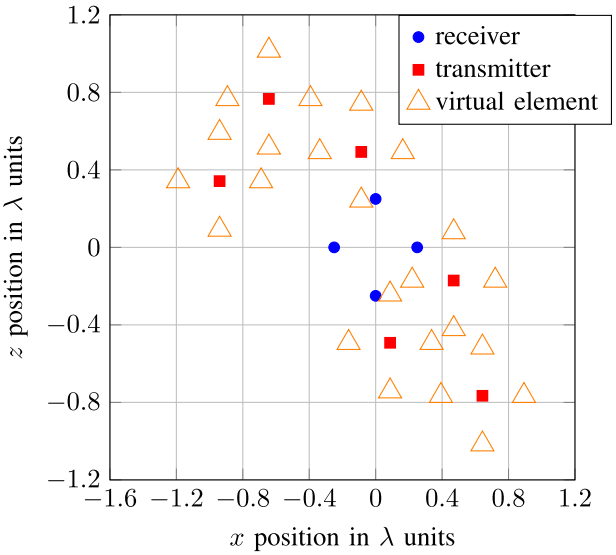

Fig. 14. Element positions of the further example of the 2-D-MIMO array with six transmitters and four receivers.

effect of these artifacts, the $\mathrm{SLL}_{\max}^m(\varphi_i^r, \vartheta_j^r)$ is obtained as the average of the local maxima in the ambiguity function matrix characterized by a correlation value greater than 0.4. In the measured case, sidelobe levels slightly higher than in the simulated case can occur. However, these values do not rise above $0.55 = -5.14$ dB. Moreover, the maximum difference between $\mathrm{SLL}_{\max}(\varphi_i^r, \vartheta_j^r)$ and $\mathrm{SLL}_{\max}^m(\varphi_i^r, \vartheta_j^r)$ is 1.7 dB. Such a difference and a ripple of around 1 dB in the measured maximum sidelobe level are due to small errors in the evaluation of the steering vector associated with the virtual array. These slight deviations are mostly caused either by reflections at the microstrip line to rectangular waveguide transitions or by a low SNR that may occur at the edges of the calibration range.

In order to add information to the comparison between the simulated and measured ambiguity function hypermatrices, the half power beamwidth values in the azimuth angle $\mathrm{HPBW}(\varphi_i^r, \vartheta_j^r)$ and $\mathrm{HPBW}^m(\varphi_i^r, \vartheta_j^r)$ for the simulated and

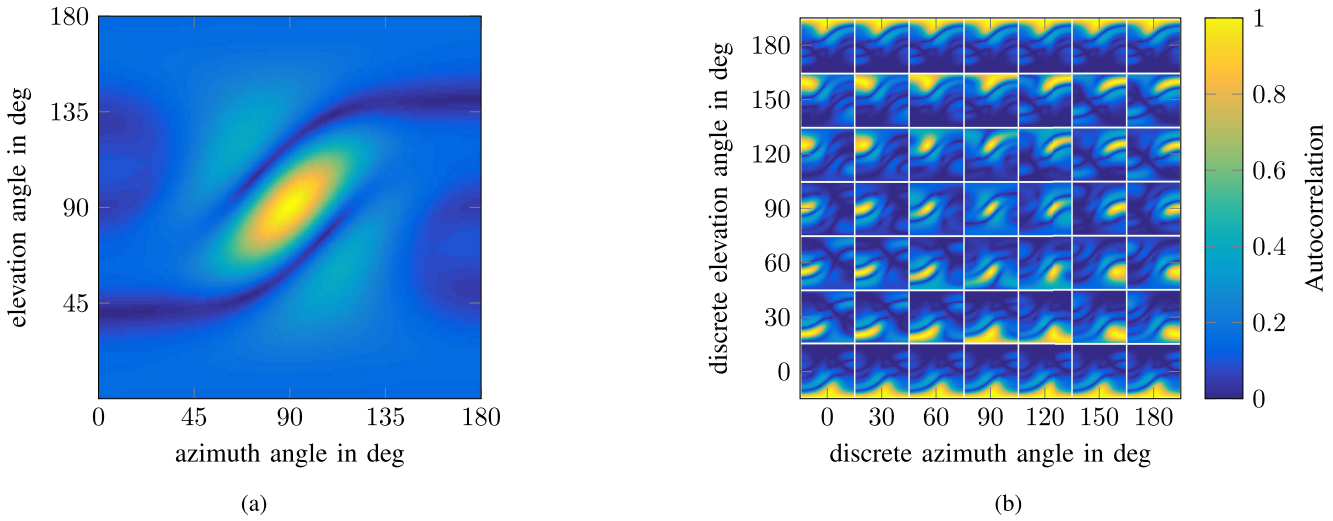

(a) (b)

Fig. 15. Ambiguity function plots associated with the further example of 2-D-MIMO sparse array with six transmitters and four receivers. (a) $\mathbf{X}(\varphi^r = 90°, \vartheta^r = 90°)$. (b) $\mathbf{H}$ with $\varphi^r, \vartheta^r \in \{0°, 30°, \ldots, 180°\}$.

measured ambiguity function matrices $\mathbf{X}_{ij}$ and $\mathbf{X}_{ij}^m$, when $50° \leq \varphi^r \leq 130°$ and $\vartheta^r = 90°$, are also analyzed. These two quantities are plotted in Fig. 13 and show a good agreement between the simulated and measured results. In fact, the simulated and measured HPBWs are mostly the same in the analyzed range. Only in few cases, localized at the edges of the analyzed range, a slight difference between them can be noticed. These small deviations, similar to the investigation conducted on the maximum sidelobe level, are due either to reflections at the microstrip line to rectangular waveguide transitions or to low SNR at the receivers. In addition, defining the error between $\mathrm{HPBW}(\varphi_i^r, \vartheta_j^r)$ and $\mathrm{HPBW}^m(\varphi_i^r, \vartheta_j^r)$ as

$$\Delta\psi(\varphi_i^r, \vartheta_j^r) = \left|\mathrm{HPBW}(\varphi_i^r, \vartheta_j^r) - \mathrm{HPBW}^m(\varphi_i^r, \vartheta_j^r)\right| \quad (15)$$

with $i = 1, \ldots, N$ and $j = 1, \ldots, M$, and defining the mean error as

$$\rho = \frac{1}{NM} \sum_{i=1}^{N} \sum_{j=1}^{M} \Delta\psi(\varphi_i^r, \vartheta_j^r) \quad (16)$$

then, under the condition above, ρ is only 0.51°.

In this contribution, thanks to the definition of the ambiguity function hypermatrix, it is possible to display all the information contained in the ambiguity function $\chi(\varphi_i^r, \vartheta_j^r, \varphi_k^e, \vartheta_l^e)$, which is a function of four variables. Further to this, unlike previous works, the measured ambiguity function matrices for DoAs different from the boresight are shown and compared to simulations, which proves the effectiveness of the proposed method for the assessment of the performance and for the optimization of 2-D-MIMO sparse arrays.

VII. Conclusion

In this article, a new approach for the performance assessment of a 2-D-MIMO radar system for 3-D-imaging based on an extensive analysis of the ambiguity function is proposed and explained in detail. The point of strength of this method is the fact that the investigation of the ambiguity function is performed in the whole angular field-of-view. In this way, the effect of possible interfering signals outside of the field-of-view of interest is considered, which improves the reliability of the results. A genetic algorithm built on the proposed approach is implemented to optimize a 2-D-MIMO sparse array composed of four transmitters and eight receivers. Considering the limited amount of array elements, the resulting array presents a significant extension of the ambiguity-free region greater than 120° in both the azimuth and elevation angles with angular resolutions of $\Delta\varphi = 8°$ and $\Delta\vartheta = 5.9°$, respectively. The antenna positions obtained from the genetic algorithm are used to realize a 2-D-MIMO array that is implemented in a radar system with an operating frequency centered at 76.5 GHz. A comparison between the simulated and measured ambiguity function hypermatrices associated with the 2-D-MIMO sparse array shows in the range $50° \leq \varphi^r \leq 130°$, $\vartheta^r = 90°$, a maximum difference between the measured and simulated maximum sidelobe levels of 1.7 dB, and the mean error ρ between the simulated and measured HPBW in the azimuth angle of only 0.51°. These results highlight a strong agreement between the simulated and measured results as well as the reliability of the proposed method.

Appendix A
Further Example of the 2-D-MIMO Array With Arbitrary Ambiguity-Free Region

In order to show the potential of the proposed approach to obtain an arbitrarily shaped ambiguity-free region, one more example of the 2-D-MIMO array is proposed. In this case, six transmitters and four receivers are considered. The 2-D-MIMO array is obtained applying a different constraint on the contiguous ambiguity-free region with respect to the one specified in Section IV. In particular, it needs to cover the whole analyzed range in the azimuth angle, i.e., $0° \leq \varphi^r \leq 180°$, while being larger than $70° \leq \vartheta^r \leq 110°$ in the elevation angle. Moreover, the constraint related to the minimum spacing between two elements is reduced to $\lambda/3$. The array element positions are

TABLE V
TRANSMITTER POSITIONS OF THE FURTHER EXAMPLE OF THE 2-D-MIMO ARRAY

i	1	2	3	4	5	6
$x_{T,i}$ in λ	-0.09	-0.94	-0.64	0.09	0.64	0.47
$z_{T,i}$ in λ	0.49	0.34	0.77	-0.49	-0.77	-0.17

TABLE VI
RECEIVER POSITIONS OF THE FURTHER EXAMPLE OF THE 2-D-MIMO ARRAY

i	1	2	3	4
$x_{R,i}$ in λ	0	0	0.25	-0.25
$z_{R,i}$ in λ	-0.25	0.25	0	0

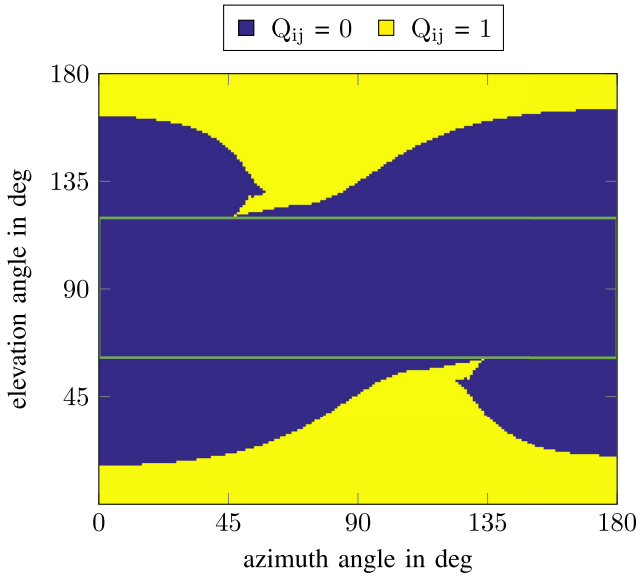

Fig. 16. Ambiguity indicator matrix **Q** of the further example of 2-D-MIMO sparse array with six transmitters and four receivers.

not limited to a discrete set. The maximum threshold for peak sidelobe levels is set to $t = 0.5 = -6$ dB.

The positions of the transmitter and receiver elements that meet this requirement are listed in Tables V and VI, respectively. The virtual array is composed by $6 \times 4 = 24$ elements and it is depicted in Fig. 14 together with the transmitter and receiver positions. The virtual apertures on the x- and z-dimensions are $d_x = 2.08\lambda$ and $d_z = 2.03\lambda$, respectively. Thus, the estimated angular resolutions of this MIMO array in the azimuth and elevation angles are $\Delta\varphi = 33.6°$ and $\Delta\vartheta = 34.4°$, respectively.

Fig. 15(a) shows the plot of the ambiguity function matrix for a real DoA at boresight $\mathbf{X}(\varphi^r = 90°, \vartheta^r = 90°)$, where the maximum sidelobe level of the ambiguity function is $\mathrm{SLL}_{\max}(90°, 90°) = 0.39 = -8.18$ dB. In Fig. 15(b), a reduced version of the ambiguity function hypermatrix **H** with $\varphi^r, \vartheta^r \in \{0°, 30°, \ldots, 180°\}$ is shown. Finally, the ambiguity indicator matrix **Q** is plotted in Fig. 16. In this case, the optimized array is characterized by a contiguous rectangular ambiguity-free region in the range $0° \leq \varphi^r \leq 180°$, $60° \leq \vartheta^r \leq 120°$, which is highlighted by the green box.

Algorithm 1 Pseudocode of the Genetic Algorithm for the Optimization of a 2-D-MIMO Sparse Array

Input: $f_c, \vartheta, \varphi, N_t, N_r, t, c_1, c_2, N_p, N_i, t_c$
Output: $\mathbf{p}_{Tx}, \mathbf{p}_{Tz}, \mathbf{p}_{Rx}, \mathbf{p}_{Rz}$
Initialization :
for $i = 1$ to N_p **do**
  while *physical constraints are not met* **do**
    generation of the random transmitter and receiver positions $\mathbf{p}_{Tx}, \mathbf{p}_{Tz}, \mathbf{p}_{Rx}, \mathbf{p}_{Rz}$
  end while
  $chromosome(i) = (\mathbf{p}_{Tx}, \mathbf{p}_{Tz}, \mathbf{p}_{Rx}, \mathbf{p}_{Rz})$
end for
Main LOOP Process
while $i \leq N_i$ **do**
  for $j = 1$ to N_p **do**
    calculation of the virtual element positions
    calculation of the associated steering vector
    calculation of the associated ambiguity function
    definition of the ambiguity indicator matrix
    evaluation of the cost function associated with the $j-th$ *chromosome*
  end for
  ascending sort of the chromosomes with respect to the cost function
  if population's maximum cost function is less than t_c **then**
    $i = N_i + 1$
  else
    discarding of the lowest half of the ranking
    generation of the new transmitter and receiver positions through pairing and mating of the chromosomes from the upper half of the ranking
    $i = i + 1$
  end if
end while
return $\mathbf{p}_{Tx}, \mathbf{p}_{Tz}, \mathbf{p}_{Rx}, \mathbf{p}_{Rz}$ *associated with the chromosome with the lowest cost function*

Contrary to the ambiguity indicator matrices in Figs. 4 and 7, it can be noticed that the ambiguity-free region in the azimuth angle is extended on the full examined range, which demonstrates the possibility to customize the optimization of the 2-D-MIMO array to application-defined requirements concerning the angular ambiguity-free region.

APPENDIX B
GENETIC ALGORITHM

In this section, the main steps of the genetic algorithm used for the optimization of the 2-D-MIMO sparse array are summarized in Algorithm 1. According to [23], the genetic algorithm itself requires three main input parameters, i.e., the number of chromosomes that form the population N_p, the maximum number of iterations N_i, and the threshold on the cost function t_c which defines the convergence condition. The remaining input parameters are used to calculate the cost function and are defined in Section II and IV of this article.

REFERENCES

[1] Y. Wang and A. E. Fathy, "Three-dimensional through wall imaging using an UWB SAR," in *Proc. IEEE Antennas Propag. Soc. Int. Symp.*, Jul. 2010, pp. 1–4.

[2] B. Cheng *et al.*, "340-GHz 3-D imaging radar with 4Tx-16Rx MIMO array," *IEEE Trans. THz Sci. Technol.*, vol. 8, no. 5, pp. 509–519, Sep. 2018.

[3] J. Grzyb, K. Statnikov, N. Sarmah, B. Heinemann, and U. R. Pfeiffer, "A 210–270-GHz circularly polarized FMCW radar with a single-lens-coupled SiGe HBT chip," *IEEE Trans. THz Sci. Technol.*, vol. 6, no. 6, pp. 771–783, Nov. 2016.

[4] Z. Peng and C. Li, "A Portable K-band 3-D MIMO radar with nonuniformly spaced array for short-range localization," *IEEE Trans. Microw. Theory Techn.*, vol. 66, no. 11, pp. 5075–5086, Nov. 2018.

[5] M. Harter, T. Mahler, T. Schipper, A. Ziroff, and T. Zwick, "2-D antenna array geometries for MIMO radar imaging by Digital Beamforming," in *Proc. Eur. Microw. Conf.*, Oct. 2013, pp. 383–386.

[6] J. M. Lopez-Sahcnez and J. Fortuny-Guasch, "3-D radar imaging using range migration techniques," *IEEE Trans. Antennas Propag.*, vol. 48, no. 5, pp. 728–737, May 2000.

[7] S. Devadithya, A. Pedross-Engel, C. M. Watts, N. I. Landy, T. Driscoll, and M. S. Reynolds, "GPU-accelerated enhanced resolution 3-D SAR imaging with dynamic metamaterial antennas," *IEEE Trans. Microw. Theory Techn.*, vol. 65, no. 12, pp. 5096–5103, Dec. 2017.

[8] C. Ma, T. S. Yeo, C. S. Tan, and Z. Liu, "Three-dimensional imaging of targets using colocated MIMO radar," *IEEE Trans. Geosci. Remote Sens.*, vol. 49, no. 8, pp. 3009–3021, Aug. 2011.

[9] X. Zhuge and A. G. Yarovoy, "Study on two-dimensional sparse MIMO UWB arrays for high resolution near-field imaging," *IEEE Trans. Antennas Propag.*, vol. 60, no. 9, pp. 4173–4182, Sep. 2012.

[10] D. Bleh *et al.*, "A 100 GHz FMCW MIMO radar system for 3D image reconstruction," in *Proc. Eur. Radar Conf. (EuRAD)*, Oct. 2016, pp. 37–40.

[11] S. Nowok, R. Herschel, R. Zimmermann, A. Shoykhetbrod, S. A. Lang, and N. Pohl, "3D imaging system based on a MIMO approach at 360GHz for security screening," in *Proc. Progr. Electromagn. Res. Symp. (PIERS)*, Aug. 2016, pp. 671–675.

[12] T. Geibig, A. Shoykhetbrod, A. Hommes, R. Herschel, and N. Pohl, "Compact 3D imaging radar based on FMCW driven frequency-scanning antennas," in *Proc. IEEE Radar Conf. (RadarConf)*, May 2016, pp. 1–5.

[13] L. Tang, H. Meng, X. Chen, J. Zhang, L. Lv, and K. Liu, "A novel 3D imaging method of FMCW MIMO-SAR," in *Proc. China Int. SAR Symp. (CISS)*, Oct. 2018, pp. 1–5.

[14] J. Dong, Q. Li, and W. Guo, "A combinatorial method for antenna array design in minimum redundancy MIMO radars," *IEEE Antennas Wireless Propag. Lett.*, vol. 8, pp. 1150–1153, 2009.

[15] K. Tan *et al.*, "On sparse MIMO planar array topology optimization for UWB near-field high-resolution imaging," *IEEE Trans. Antennas Propag.*, vol. 65, no. 2, pp. 989–994, Feb. 2017.

[16] J. L. Schwartz and B. D. Steinberg, "Ultrasparse, ultrawideband arrays," *IEEE Trans. Ultrason., Ferroelectr., Freq. Control*, vol. 45, no. 2, pp. 376–393, Mar. 1998.

[17] O. Lange and B. Yang, "Antenna geometry optimization for 2D direction-of-arrival estimation for radar imaging," in *Proc. Int. ITG Workshop Smart Antennas*, Feb. 2011, pp. 1–8.

[18] M. Ulrich, Y. Yang, and B. Yang, "Design of multi-carrier MIMO radar array for DOA estimation," in *Proc. 25th Eur. Signal Process. Conf. (EUSIPCO)*, Aug. 2017, pp. 1957–1961.

[19] M. Eric, A. Zejak, and M. Obradovic, "Ambiguity characterization of arbitrary antenna array: Type I ambiguity," in *Proc. IEEE 5th Int. Symp. Spread Spectr. Techn. Appl. Spread Technol. Afr.*, vol. 2, Sep. 1998, pp. 399–403.

[20] J. Li and P. Stoica, *MIMO Radar Signal Processing*. Hoboken, NJ, USA: Wiley, 2008.

[21] W.-H. Steeb and T. K. Shi, *Matrix Calculus and Kronecker Product with Applications and C++ Programs*. Singapore: World Scientific, 1997.

[22] L. Rayleigh, "XXXI. Investigations in optics, with special reference to the spectroscope," *Philos. Mag.*, vol. 8, no. 49, pp. 261–274, 1879.

[23] R. L. Haupt, "An introduction to genetic algorithms for electromagnetics," *IEEE Antennas Propag. Mag.*, vol. 37, no. 2, pp. 7–15, Apr. 1995.

[24] P. Hugler, F. Roos, M. Schartel, M. Geiger, and C. Waldschmidt, "Radar taking off: New capabilities for UAVs," *IEEE Microw. Mag.*, vol. 19, no. 7, pp. 43–53, Nov. 2018.

[25] H. Rohling, "Radar CFAR thresholding in clutter and multiple target situations," *IEEE Trans. Aerosp. Electron. Syst.*, vol. AES-19, no. 4, pp. 608–621, Jul. 1983.

Adolfo Di Serio (Student Member, IEEE) received the M.Sc. degree in communication engineering from the University of Salento, Lecce, Italy, in 2016. He is currently pursuing the Ph.D. degree with the Institute of Microwave Engineering, Ulm University, Ulm, Germany.

Since 2018, he has been a Research Assistant with the Institute of Microwave Engineering, Ulm University. From 2016 to 2017, he was first an Intern and then a Research Assistant with the Wireless Sensor Network Group, Tyndall National Institute, Cork, Ireland. In 2015, he spent a semester as an Exchange Student at the Institute of Microwave Engineering, Ulm University. His actual research interest is focused on the system design of imaging radar sensors in the sub-THz frequency range.

Philipp Hügler (Student Member, IEEE) received the M.Sc. degree in electrical engineering from Ulm University, Ulm, Germany, in 2014, where he is currently pursuing the Ph.D. degree with the Institute of Microwave Engineering (MWT).

His research focuses on close-up range FMCW radar sensors and imaging radar front ends at millimeter-wave frequencies for UAV applications.

Fabian Roos (Student Member, IEEE) received the M.Sc. degree in electrical engineering and information technology from the Karlsruhe Institute of Technology (KIT), formerly Universität Karlsruhe, Karlsruhe, Germany, in 2014. He is currently pursuing the Ph.D. degree with Ulm University, Ulm, Germany.

Since September 2014, he has been a Research Assistant with Ulm University. His research interests include automotive radar and environmental perception with a focus on adaptivity for chirp-sequence-modulated automotive radar sensors.

Christian Waldschmidt (Senior Member, IEEE) received the Dipl.-Ing. (M.S.E.E.) and Dr.-Ing. (Ph.D.E.E.) degrees from University Karlsruhe (TH), Karlsruhe, Germany, in 2001 and 2004, respectively.

From 2001 to 2004, he was a Research Assistant with the Institut für Höchstfrequenztechnik and Elektronik (IHE), TH. Since 2004, he has been with Robert Bosch GmbH, Gerlingen, Germany, in the business units Corporate Research and Chassis Systems. He was heading different research and development teams in microwave engineering, RF-sensing, and automotive radar. In 2013, he returned to academia. He was appointed as the Director of the Institute of Microwave Engineering, Ulm University, Ulm, Germany, as a Full Professor. He authored or coauthored over 200 scientific publications and holds more than 20 patents. The research topics focus on radar and RF sensing, mm-wave and submillimeter-wave engineering, antennas and antenna arrays, RF, and array signal processing.

Dr. Waldschmidt is a member of the Executive Committee Board of the German MTT/AP Joint Chapter and the German Information Technology Society (ITG). He has been a co-recipient of 11 best paper awards since 2014. He served as the Chair for the IEEE MTT-27 Technical Committee on wireless-enabled automotive and vehicular applications. He was the two-time TPC Chair and the General Chair of the IEEE MTT International Conference on Microwaves for Intelligent Mobility. Since 2018, he has been serving as an Associate Editor for the IEEE MTT MICROWAVE WIRELESS COMPONENTS LETTERS (MWCL). He is a reviewer for multiple IEEE TRANSACTIONS and many IEEE conferences in the field of microwaves.